# Authentic Enzyme Intermediates Captured "on-the-fly" by Mix-and-Inject Serial Crystallography

Jose Olmos[#,a], Suraj Pandey[#,b], Jose M. Martin-Garcia[#,c], George Calvey[d], Andrea Katz[d], Juraj Knoska[e,f], Christopher Kupitz[b], Mark S. Hunter[g], Mengning Liang[g], Dominik Oberthuer[e], Oleksandr Yefanov[e], Max Wiedorn[e,f], Michael Heyman[h], Mark Holl[c], Kanupriya Pande[i], Anton Barty[e], Mitchell D. Miller[a], Stephan Stern[e], Shatabdi Roy-Chowdhury[c], Jesse Coe[c], Nirupa Nagaratnam[c], James Zook[c], Jacob Verburgt[b], Tyler Norwood[b], Ishwor Poudyal[b], David Xu[a], Jason Koglin[g], Matt Seaberg[g], Yun Zhao[c], Saša Bajt[j], Thomas Grant[k], Valerio Mariani[e], Garrett Nelson[l], Ganesh Subramanian[l], Euiyoung Bae[m], Raimund Fromme[c], Russel Fung[b], Peter Schwander[b], Matthias Frank[n], Thomas White[e], Uwe Weierstall[i], Nadia Zatsepin[i], John Spence[i], Petra Fromme[c], Henry N. Chapman[e,f,o], Lois Pollack[d], Lee Tremblay[p], Abbas Ourmazd[b], George N. Phillips, Jr.[a], Marius Schmidt[b,*]

[a]Department of BioSciences, Rice University, 6100 Main Street, Houston, Texas 77005, USA
[b]Physics Department, University of Wisconsin-Milwaukee, 3135 N. Maryland Ave, Milwaukee, Wisconsin 53211, USA
[c]School of Molecular Sciences and Biodesign Center for Applied Structural Discovery, Arizona State University, Tempe, Arizona 85287-1604, USA
[d]Department of Applied and Engineering Physics, Cornell University, 254 Clark Hall, Ithaca, New York 14853, USA
[e]Center for Free-Electron Laser Science, DESY, Notkestrasse 85, 22607 Hamburg, Germany
[f]University of Hamburg, Luruper Chaussee 149, 22761 Hamburg, Germany
[g]Linac Coherent Light Source, Stanford Linear Accelerator Center (SLAC) National Accelerator Laboratory, 2575 Sand Hill Road, Menlo Park, California 94025, USA
[h]Max Planck Institut fuer Biochemie, Am Klopferspitz 18, 82152 Planegg, Germany
[i]Lawrence Berkeley National Lab, 1 Cyclotron Road, Berkeley CA 94720
[j]Photon Science, DESY, Notkestrasse 85, 22607 Hamburg, Germany
[k]University of New York Buffalo, Hauptman-Woodward Institute, 700 Ellicott St, Buffalo, NY 14203, USA.
[l]Department of Physics, Arizona State University, Tempe, Arizona 85287, USA
[m]Department of Agricultural Biotechnology, Seoul National University, Seoul 151-921, Korea
[n]Lawrence Livermore National Laboratory, Livermore, CA 94550, USA
[o]Centre for Ultrafast Imaging, Luruper Chaussee 149, 22761 Hamburg, Germany
[p]4Marbles Inc., 1900 Belvedere Pl, Westfield, Indiana 46074, USA

[#]contributed equally
*correspondence to m-schmidt@uwm.edu

**Synopsis.** An enzymatically catalyzed reaction is initiated by diffusion based mixing of substrate and followed at runtime by TR-SFX at an XFEL.

Ever since the first structure of an enzyme was solved, the discovery of the mechanism and dynamics of reactions catalyzed by biomolecules has been the key goal for the understanding of the molecular processes that drive life on earth at the atomic scale. Despite a large number of successful methods for trapping reaction intermediates, the direct observation of an ongoing reaction at runtime has been possible only in rare and exceptional cases. Here, we demonstrate a general method for capturing enzyme catalysis 'in action' by 'mix-and-inject serial crystallography'. Specifically, we follow the catalytic reaction of the *Mycobacterium tuberculosis* β-lactamase with the 3rd generation antibiotic ceftriaxone by time-resolved serial femtosecond crystallography. The results reveal, in near atomic detail, antibiotic cleavage and inactivation on the millisecond to second time scales including the crossover from transition state kinetics to steady-state kinetics.

Observing the catalytic action of a biomolecule in atomic detail has been the dream of structural biologists since the first structure of an enzyme was solved (*2, 3*). By exploiting X-ray radiation from powerful synchrotron sources, time-resolved crystallographic methods were developed (*4*) with the goal to achieve a complete description of a reaction in real time (*5, 6*). However, X-ray damage and the need for large single crystals made time-resolved crystallography very challenging. The advent of X-ray Free Electron Lasers (XFELs) enabled time resolved serial femtosecond (fs) crystallography, where X-ray damage is outrun by ultrashort fs X-ray pulses (*7, 8*). This approach made it possible to follow and describe cyclic (reversible) reactions that can be triggered by light. Examples include pioneering studies that investigate the photocycle in the photactive yellow protein (*9, 10*), myoglobin (*11*), or photosystem II (*12-15*). However, structural investigations on one-pathway (irreversible) enzymatic reactions present additional difficulties, because diffusion of substrate(s) and products in and out of the crystals limit the accessible reaction times. Standard crystallography can be used to track reaction intermediates of slow reaction by flash freezing but is unable to study enzymatic reactions at room temperature in real time. The largest problem, however, is to start a reaction in large sized crystals; initiation by diffusion is far slower than the typical millisecond turnover times of enzymes. It was proposed that one can trigger enzymatic reactions by light by soaking inactive (caged) substrates (*16*) into the crystals, which can be activated for example by a laser pulse. The first proof of concept for TR-Laue crystallography triggered by a caged substrate was achieved in 1990 (*17*). While this method has great potential, its application has so far been limited due to significant

experimental challenges. Only a few time-resolved experiments have been reported where highly reactive, caged substrates are readily available (*17-19*), or the reactions are slow to allow the use of conventional, monochromatic methods (*20, 21*). It is therefore highly desirable to develop new methods that open the field of time-resolved crystallography to the study of biomolecular reactions at room temperature with the native enzyme and its natural substrate(s). Structural studies at XFELs provide a breakthrough. The XFEL intensity is high enough to generate a diffraction pattern from an exposure to a single fs X-ray pulse even from micron and submicron sized crystals. These tiny crystals allow for fast diffusion times which are not rate limiting (*22-27*). The nanocrystals are mixed "on the fly" and injected into the XFEL beam, a method we call "mix-and-inject serial crystallography" (MISC) (*24, 26*). In MISC, crystals react with their native substrate(s) at ambient temperature until they are intercepted (probed) the by a single X-ray pulse, which destroys them only after diffraction data has been recorded. The pulses are short enough to essentially outrun radiation damage by means of the "diffraction-before-diffraction" principle (*28-30*). Optimized injectors have been recently developed (*31, 32*) for MISC experiments with the potential to provide submillisecond time resolution (*33*). The microcrystals tolerate even larger conformational changes leading to unit cell or even space group changes (*12, 27*).

Here, we apply MISC to the study of a very important public-health problem: antibiotic resistance of bacteria. Specifically, we have obtained time-resolved crystallographic data on the binding and cleavage of the third-generation antibiotic ceftriaxone (CEF) in microcrystals of the enzyme β-lactamase from *M. tuberculosis* (BlaC). In these experiments carried out at the Linac Coherent Light Source (LCLS) BlaC

micro-crystals are mixed with CEF on the fly, and the cleavage and thereby inactivation of the antibiotics by β-lactamase is followed in runtime. BlaC is a broad-spectrum β-lactamase which provides tuberculosis with resistance to all classes of β-lactam antibiotics. BlaC chemistry has rendered the frontline arsenal of antibacterial agents ineffective against this deadly disease, creating a global public health crisis. More generally, our approach is applicable to broad classes of important enzymes with the potential to fundamentally alter our understanding of the molecular basis of biomolecular reactions vital to the design of novel drugs.

Beginning with the famous discovery of penicillin, β-lactam antibiotics were widely used to eliminate deadly infectious diseases (*34*). More compounds with diverse chemical composition were found through the years (*35*), the most prominent of them are most likely the cephalosporins. The chemical structure of CEF is shown in Scheme 1. Unlike the penicillins which feature a 5-membered thiazolidine ring, in the chephalosporins a 6-membered dihydrothiazine ring is fused to the β–lactam ring (1). However, resistance against these antibiotics was observed shortly after their widespread use, and is now rampant. β-lactamases open the β-lactam ring rendering the antibiotic inactive. BlaC from *M. tuberculosis*, an Ambler class A β-lactamase (*36*), uses a conserved serine to attack the β-lactam ring (scheme 1, blue arrow) thus inactivating the antibiotics. Because of the great medical challenge that BlaC causes for the fight against infectious diseases the process of catalysis has been studied by conventional biochemcial methods in detail leading to the hypothesis of a three step model of the cleavage process: The first step is the formation of the enzyme-substrate complex (1), and it has been proposed that the enzyme may use active site interactions to orient the β-lactam carbonyl-carbon near the

Ser-70 nucleophile (*37, 38*). The next step proposed along the reaction coordinate is the opening of the β-lactam ring subsequently or concurrently with formation of the covalently bound active site acyl-intermediate (3). For cephalosporins there is evidence that during the enzymatic reaction a release group (denoted $R_2$ in Scheme 1) is split off (*39*). In the third step, the open-ring β-lactam is hydrolyzed and leaves the enzyme. Various rates have been reported for this step of the catalytic reaction across different classes of β-lactams, followed by product release (*37*). Obtaining time-resolved data on BlaC chemistry holds the potential to directly visualize substrate chemical intermediates and the accompanying active site interactions, for wide-ranging implications for all classes of β-lactams. Ultimately, knowledge of the physical processes by which BlaC is able to bind and catalyze the breakdown of β-lactams, will directly impact rational drug design against deadly human diseases.

Our previous results showed that CEF can diffuse into the crystals and binds to the active site of the tetrameric β-lactamase (*26*). These first studies showed that the catalytic reaction is heterogeneous as the reactivity is specific to individual subunits in the β-lactamase tetramer. Only subunits B and D bind and process CEF, while subunits A and C do not directly contribute to catalysis. However, this first proof of concept study was limited to a single time point about 2 s after reaction initiation. Multiple time points that cover the reaction are required. Here we present time series from 30 ms to 2 s after mixing with substrate in two crystal forms, shards and needles, which allow us to discover the conformational changes and to characterize the kinetics of this important class of enzymes directly from the X-ray data.

One of the critical questions in MISC concerns whether the enzyme in the crystals is still catalytically active and whether the reaction is limited by constraints of crystal packing or the solvent/precipitant used for crystallization. We have therefore crystallized BlaC in two different crystal forms. With phosphate as precipitant, the BlaC crystallizes in a shard-shaped crystal form with a tetramer in the asymmetric unit (Fig. 1a) as previously reported (*26*). With PEG 1000 as precipitant, needle shaped crystals are obtained with a monomer in the asymmetric unit (see also the supplemental material, SM, provided online). The packing of BlaC in both crystal forms is shown in Fig. S3. In our MISC experiment, the small microcrystals were rapidly mixed with CEF 'on the fly' using highly optimized mixing devices (SM), and structures of the reaction of BlaC with CEF were determined by scattering from femtosecond X-ray pulses at four time points (30 ms, 100 ms, 500 ms, and 2 s after mixing, respectively) during the reaction in both crystal forms. Results are shown in Figs. 1 and 2. CEF binds to the active site of BlaC as shown in Fig. 1a, and in Fig. 2 more details are shown for the substrate binding in the shards and needles crystal forms. Our results show that the formation of the enzyme-substrate complex (ES) can be observed within 30 ms (Fig. 2 a,b,c). This is followed by the attack of Ser-70 which opens the β-lactam ring. At the same time,the release group is split off, which leads to the formation of a covalently bound shorter ligand denoted CFO. There are subtle differences between the results from the two crystal forms, and even between subunits (Fig. 2), confirming previous preliminary observations (*26*). In both crystal forms, at 100 ms a substantial fraction (~70%, see also Tab. S2) of CEF molecules are still intact. A minor fraction (~30%) has an open β-lactam ring (Fig. 2d,e,f). The open species CFO can be identified more clearly at 500 ms, where it dominates (70%) the electron density.

This confirms, for the first time on a structural basis, previous predictions from biochemical results for other cephalosporin species (*39*). The red arrow in Fig. 2g indicates that the double bond Δ (Scheme 1) has reacted to an alcohol in subunit B. This behavior is not seen in subunit D, nor in the needle form of the crystals. At 2 s, the structures reveal the steady state of the enzyme, where the binding sites are occupied mainly by the full length CEF with minor contribution from CFO (< 20%) in the shards.

In the shards crystal from, subunits A and C do not directly participate in catalysis, at least not in the first 2 s. In the needles it appears that the reaction proceeds similarly to that observed in subunit D in the shards. However, substrate occupancy is lower compared to that in the shards, with substoichiometric occupation ranging from 20 % - 40 %. The reason for this might be that the enzyme concentration in the needles is very high, 30 mmol/L (~ 940 mg/mL). In the shards it is only 16 mmol/L (~ 510 mg/mL). To reach full occupation in the needles, obviously at least 30 mmol/L of CEF (one CEF molecule per asymmetric unit) is initially required, which needs to be delivered by diffusion from the solution to the side of the crystal. While the outside CEF concentration is on the order of 200 mmol/L in both experiments, the ratio of CEF to enzyme varies in the shards and needles crystals forms. Fig. S3 shows how the solvent volume that contains CEF surrounding the BlaC molecules in the crystals varies. Where it is on the order of 65% for the shards it is substantially lower (38%) in the needles. Fig. S3 also shows that there are substantial differences in the solvent channel sizes in the two crystal forms. Both may significantly impact diffusion of substrate into the crystals. However, CEF is a slow binder (see discussion in the SM). The reaction initiation does not critically depend on the

diffusion time of the substrate (Fig. 3). Accordingly, the reaction dynamics of the catalytic reaction in the needles and the shards crystal forms are similar.

An additional CEF molecule ($CEF^{stack}$) can be identified near the catalytic clefts of subunits B and D, each, in the shards crystal form (Fig. 1a,b,c). This molecule stacks to the CEF species that occupy the active sites on all time scales. $CEF^{stack}$ is non-covalently attached to Arg-126 and Tyr-127 of the subunits A or C, which are adjacent to the active catalytic clefts of subunits B or D, respectively (more details are listed in the SM). This way $CEF^{stack}$ is pre-oriented, and can rapidly access the active site after CFO has been hydrolyzed and left the enzyme. Since stacking is not observed in the monomeric needle crystal form, it might be argued that it represents a non-physiological, nonspecifically bound substrate that occurs only in BlaC dimers and that dimers exist only in crystals. Previous studies showed that BlaC can crystallize in monomeric form (*38*) as in our needles. Others (*1*) report crystal forms with a tetramer (dimer of dimers) in the asymmetric unit as in our shards. Dynamic light scattering (Fig. S4) and size exclusion chromatography (not shown) performed on the BlaC at pH 5 show that BlaC exists predominantly as dimers at this pH, irrespective of the buffer and the concentration. For the BlaC it appears that the oligomerization state in the crystals is selected by the crystallization buffer. Since, after infection, *M. tuberculosis* resides in the macrophages at pH values near 4.5 (*40*), the BlaC dimer is most likely the physiologically relevant form. The interesting question of the physiological oligomeric state of the BlaC warrants further investigation. The binding of the additional CEF molecule could be an important mechanism to steer the substrate towards, and orient it with respect to, the active site. It appears that at the very high concentrations of CEF applied here, stacking is not required

for effective catalysis, as the kinetics in the monomeric needles, where stacking does not occur, is similar to that in the tetrameric shard crystal form. However, when only small CEF concentrations are present, stacking might well be essential to recruit antibiotic substrate molecules to promote effective BlaC function.

One of the major questions addressed here is whether the structural data obtained by MISC can be interpreted in accordance with previous investigations on BlaC catalysis. A compatible chemical, kinetic mechanism must be developed and expressed in the standard terminology of enzyme kinetics (*41, 42*). Accordingly we simulated the catalytic cycle of BlaC using literature values of the Michaelis constant $K_m$ (~500 μmol/L) and $k_{cat}$ (0.8 1/s) (*37*). We further assumed a sufficiently large number of intermediate states in our mechanism to explain our observations (see the SM for further description). Our simulations describe the change from the transient state regime at 30 ms to the steady state regime at 2 s, and covers a large range of substrate and product concentrations (Fig. 3). We then compared the simulations to our MISC experiment. Since only 4 time delays are available, the parameters in the mechanism can not be determined fully quantitatively, but the simulations reproduce the experimental observations. After initial formation of the enzyme-substrate (ES) complex represented by a non-covalently bound full length CEF, an enzyme-product species (EP) with a covalently bound CFO has its peak concentration at 500 ms. It has been previously suggested (*38*) that the hydrolytic cleavage of an acyl-adduct from Ser-70 (hydrolysis of species 4 in scheme 1) should be, if any, the rate limiting process of BlaC catalysis. Then the EP species should be the dominant species in the steady state (2 s). However, this is not the case as the ES complex with the non-covalently bound, full length CEF is prevalent (> 70%) in our MISC

data at 2 s. This can be explained by the simulation, if the nucleophilic attack of Ser-70 on species (2) in scheme 1 is inhibited, or slowed down. Since high product concentrations of > 10 mmol/L are reached already after one catalytic cycle due to the very high enzyme and substrate concentrations, product inhibition is plausible. Its structural mechanism, however, remains unknown (see also the SM). After an initial burst over the first second, the nucleophilic attack by Ser-70 becomes the rate-limiting process, and the ES complex accumulates in the steady state as observed in our X-ray data.

Our results show that structural characterization of enzymatically catalyzed reactions on the millisecond time scale is now possible. With more conventional X-ray sources, radiation damage prevents the collection of even a single diffraction pattern (*43*) from these small crystals. These difficulties are circumvented by the ultra-short, brilliant hard X-ray pulses available at XFELs. MISC (*26*) can now be employed to investigate a large number of non-cyclic (single pass) reactions in proteins and enzymes, some of which are of immense biological importance, and might be, in addition, important targets for structure based drug design. With MHz X-ray pulse rates expected at LCLS-II and the European XFEL, multiple, finely spaced time delays may be collected rapidly to allow for a comprehensive description of the biomolecular reaction in terms of structure and kinetics. In the future, with further advances and more XFELs worldwide, enzymology might become predominantly structure based.

**Acknowledgements.**

This work was supported the NSF-STC “BioXFEL” through award STC-1231306, and in part by the US Department of Energy, Office of Science, Basic Energy Sciences, under contract DE-SC0002164 (A.O., algorithm design and development) and by the NSF under

contract number 1551489 (A.O., underlying analytical models). This material is based upon work supported by the National Science Foundation Graduate Research Fellowship Program to J.L.O. under Grant No. 1450681. The work was also supported by funds from the National Institutes of Health grants R01 GM117342-01 and R01 GM095583, by funds from the Biodesign Center for Applied Structural Discovery at ASU, and the U.S. Department of Energy through Lawrence Livermore National Laboratory under contract DE-AC52-07NA27344. Part of this work was also supported by program-oriented funds of the Helmholtz Association. The structures and diffraction data of the BlaC, unmixed and mixed with Ceftriaxone at 0 s, 30 ms, 100 ms, 500 ms and 2 s for shards and needles crystal forms are deposited to the pdb with the following access codes. Shards: 6B5X (unmixed), 6B5Y (30 ms), 6B68 (100 ms), 6B69 (500 ms), 6B6A (2 s). Needles: 6B6B (unmixed), 6B6C (30 ms), 6B6D (100 ms), 6B6E (500 ms), 6B6F (2s).

**Author Contributions.**

J.O, J.M.M-G., C.K., D.O., M.D.M., N.N., J.Z.,T.N., D.X., E.B., R.F., L.T., G.N.P., Mar.S. prepared and crystallized samples. M.S.H., M. L., J.K., Mat.S. operated the CXI beamline. A.K., G.C., J.K., D.O., M.W., M.H.,S.S., S.R-C.,J.C., N.N., J.Z., Y.Z., G.N., S.B., U.W., H.N.C., L.P. provided the injector systems, and operated injection at the CXI beamline. S.P., D.O., O.Y., K.P., A.B., T.N., I.P., T.G., V.M., G.S., R.F., P.S., M.F., T.W., N.Z. collected and processed the data. J.O., S.P., J.M.M-G, C.K., D.O., M.H., M.D.M., T.N., I.P., D.X., R.F., P.F., G.N.P., Mar.S. analyzed and interpreted the data. L.T., A.O, Mar.S. conceived the project. P.F., A.O., G.N.P., Mar.S. wrote the manuscript with contributions from all authors.

**Literature**


1. F. Wang, C. Cassidy, J. C. Sacchettini, Crystal structure and activity studies of the Mycobacterium tuberculosis beta-lactamase reveal its critical role in resistance to beta-lactam antibiotics. *Antimicrobial agents and chemotherapy* **50**, 2762-2771 (2006).
2. C. C. Blake *et al.*, Structure of hen egg-white lysozyme. A three-dimensional Fourier synthesis at 2 Angstrom resolution. *Nature* **206**, 757-761 (1965).
3. L. N. Johnson, D. C. Phillips, Structure of some crystalline lysozyme-inhibitor complexes determined by X-ray analysis at 6 Angstrom resolution. *Nature* **206**, 761-763 (1965).
4. K. Moffat, Time-resolved macromolecular crystallography. *Annu Rev Biophys Biophys Chem* **18**, 309-332 (1989).
5. M. Schmidt, *Structure Based Enzyme Kinetics by Time-Resolved X-ray crystallography, in: Ultrashort Laser Pulses in Medicine and Biology*. W. Zinth, M. Braun, P. Gilch, Eds., Biological and medical physics, biomedical engineering, ISSN 1618-7210 (Berlin ; New York : Springer, c2008, Germany, 2008).
6. M. Schmidt, Time-Resolved Macromolecular Crystallography at Modern X-Ray Sources. *Methods Mol Biol* **1607**, 273-294 (2017).
7. S. Boutet *et al.*, High-resolution protein structure determination by serial femtosecond crystallography. *Science* **337**, 362-364 (2012).
8. G. Chreifi *et al.*, Crystal structure of the pristine peroxidase ferryl center and its relevance to proton-coupled electron transfer. *Proceedings of the National Academy of Sciences of the United States of America* **113**, 1226-1231 (2016).
9. K. Pande *et al.*, Femtosecond Structural Dynamics Drives the Trans/Cis Isomerization in Photoactive Yellow Protein. *Science* **352**, 725-729 (2016).
10. J. Tenboer *et al.*, Time-resolved serial crystallography captures high-resolution intermediates of photoactive yellow protein. *Science* **346**, 1242-1246 (2014).
11. T. R. Barends *et al.*, Direct observation of ultrafast collective motions in CO myoglobin upon ligand dissociation. *Science*, (2015).
12. C. Kupitz *et al.*, Serial time-resolved crystallography of photosystem II using a femtosecond X-ray laser. *Nature* **513**, 5 (2014).
13. J. Kern *et al.*, Simultaneous femtosecond X-ray spectroscopy and diffraction of photosystem II at room temperature. *Science* **340**, 491-495 (2013).
14. I. D. Young *et al.*, Structure of photosystem II and substrate binding at room temperature. *Nature* **540**, 453-457 (2016).
15. M. Suga *et al.*, Light-induced structural changes and the site of O=O bond formation in PSII caught by XFEL. *Nature* **543**, 131-135 (2017).
16. M. Goelder, R. Givens, *Dynamic Studies in Biology: Phototriggers, Photoswitches and Caged Biomolecules*. (Wiley VCH, 2005).
17. I. Schlichting *et al.*, Time-Resolved X-Ray Crystallographic Study of the Conformational Change in Ha-Ras P21 Protein on Gtp Hydrolysis. *Nature* **345**, 309-315 (1990).
18. D. Bourgeois, M. Weik, Kinetic protein crystallography: a tool to watch proteins in action. *Crystallogr Rev* **15**, 87-118 (2009).

19. B. L. Stoddard, B. E. Cohen, M. Brubaker, A. D. Mesecar, D. E. Koshland, Jr., Millisecond Laue structures of an enzyme-product complex using photocaged substrate analogs. *Nat Struct Biol* **5**, 891-897 (1998).
20. J. R. Helliwell *et al.*, Time-resolved structures of hydroxymethylbilane synthase (Lys59Gln mutant) as it is loaded with substrate in the crystal determined by Laue diffraction. *J Chem Soc Faraday T* **94**, 2615-2622 (1998).
21. T. H. Kim *et al.*, The role of dimer asymmetry and protomer dynamics in enzyme catalysis. *Science* **355**, (2017).
22. L. A. Sluyterman, M. J. de Graaf, The activity of papain in the crystalline state. *Biochimica et biophysica acta* **171**, 277-287 (1969).
23. S. Geremia, M. Campagnolo, N. Demitri, L. N. Johnson, Simulation of diffusion time of small molecules in protein crystals. *Structure* **14**, 393-400 (2006).
24. M. Schmidt, Mix and Inject, Reaction Initiation by Diffusion for Time-Resolved Macromolecular Crystallography. *Advances on Condensed Matter Physics*, 1-10 (2013).
25. J. Hajdu *et al.*, Analyzing protein functions in four dimensions. *Nat Struct Biol* **7**, 1006-1012 (2000).
26. C. Kupitz *et al.*, Structural enzymology using X-ray free electron lasers. *Struct Dyn* **4**, 044003 (2017).
27. J. R. Stagno *et al.*, Structures of riboswitch RNA reaction states by mix-and-inject XFEL serial crystallography. *Nature* **541**, 242-246 (2017).
28. H. N. Chapman *et al.*, Femtosecond X-ray protein nanocrystallography. *Nature* **470**, 73-77 (2011).
29. L. Lomb *et al.*, Radiation damage in protein serial femtosecond crystallography using an x-ray free-electron laser. *Physical review. B, Condensed matter and materials physics* **84**, 214111 (2011).
30. H. N. Chapman *et al.*, Femtosecond diffractive imaging with a soft-X-ray free-electron laser. *Nat Phys* **2**, 839-843 (2006).
31. G. D. Calvey, A. M. Katz, C. B. Schaffer, L. Pollack, Mixing injector enables time-resolved crystallography with high hit rate at X-ray free electron lasers. *Struct Dyn* **3**, 054301 (2016).
32. D. Oberthuer *et al.*, Double-flow focused liquid injector for efficient serial femtosecond crystallography. *Scientific reports* **7**, 44628 (2017).
33. D. Wang, U. Weierstall, L. Pollack, J. Spence, Liquid Mixing Jet for XFEL Study of Chemical Kinetics. *J. Synchrotron Rad.* **21**, 1364-1366 (2014).
34. K. F. Kong, L. Schneper, K. Mathee, Beta-lactam antibiotics: from antibiosis to resistance and bacteriology. *APMIS* **118**, 1-36 (2010).
35. M. Bassetti, M. Merelli, C. Temperoni, A. Astilean, New antibiotics for bad bugs: where are we? *Ann Clin Microbiol Antimicrob* **12**, 22 (2013).
36. R. P. Ambler, The structure of beta-lactamases. *Philosophical transactions of the Royal Society of London. Series B, Biological sciences* **289**, 321-331 (1980).
37. J. E. Hugonnet, J. S. Blanchard, Irreversible inhibition of the Mycobacterium tuberculosis beta-lactamase by clavulanate. *Biochemistry* **46**, 11998-12004 (2007).

38. L. W. Tremblay, F. Fan, J. S. Blanchard, Biochemical and structural characterization of Mycobacterium tuberculosis beta-lactamase with the carbapenems ertapenem and doripenem. *Biochemistry* **49**, 3766-3773 (2010).
39. D. B. Boyd, W. H. Lunn, Electronic structures of cephalosporins and penicillins. 9. Departure of a leaving group in cephalosporins. *J Med Chem* **22**, 778-784 (1979).
40. O. H. Vandal, C. F. Nathan, S. Ehrt, Acid resistance in Mycobacterium tuberculosis. *J Bacteriol* **191**, 4714-4721 (2009).
41. A. Cornish-Bowden, *Fundamentals of Enzyme Kinetics*. (Wiley-VCH, ed. 4 edition, 2012).
42. J. I. Steinfeld, J. S. Francisco, W. L. Hase, *Chemical Kinetics and Dynamics*. (Prentience Hall, ed. 2 edition, 1985).
43. J. M. Holton, K. A. Frankel, The minimum crystal size needed for a complete diffraction data set. *Acta Crystallogr D* **66**, 393-408 (2010).
44. R. A. Kirian *et al.*, Structure-factor analysis of femtosecond microdiffraction patterns from protein nanocrystals. *Acta crystallographica. Section A, Foundations of crystallography* **67**, 131-140 (2011).
45. T. A. White *et al.*, CrystFEL: a software suite for snapshot serial crystallography. *J Appl Crystallogr* **45**, 335-341 (2012).
46. S. Boutet, G. J. Williams, The Coherent X-ray Imaging (CXI) instrument at the Linac Coherent Light Source (LCLS). *New J Phys* **12**, (2010).
47. A. Barty *et al.*, Cheetah: software for high-throughput reduction and analysis of serial femtosecond X-ray diffraction data. *J Appl Crystallogr* **47**, 1118-1131 (2014).
48. T. A. White *et al.*, Recent developments in CrystFEL. *J Appl Crystallogr* **49**, 680-689 (2016).
49. R. D. Oeffner, G. Bunkoczi, A. J. McCoy, R. J. Read, Improved estimates of coordinate error for molecular replacement. *Acta Crystallogr D* **69**, 2209-2215 (2013).
50. T. C. Terwilliger *et al.*, Iterative-build OMIT maps: map improvement by iterative model building and refinement without model bias. *Acta crystallographica. Section D, Biological crystallography* **64**, 515-524 (2008).
51. A. Hodel, S. H. Kim, A. T. Brunger, Model Bias in Macromolecular Crystal-Structures. *Acta Crystallographica Section A* **48**, 851-858 (1992).
52. P. D. Adams *et al.*, PHENIX: a comprehensive Python-based system for macromolecular structure solution. *Acta crystallographica. Section D, Biological crystallography* **66**, 213-221 (2010).
53. P. Emsley, B. Lohkamp, W. G. Scott, K. Cowtan, Features and development of Coot. *Acta crystallographica. Section D, Biological crystallography* **66**, 486-501 (2010).
54. M. R. Majidi, K. Asadpour-Zeynali, B. Hafezi, Electrocatalytic oxidation and determination of ceftriaxone sodium antibiotic in pharmaceutical samples on a copper hexacyanoferrate nanostructure. *Anal Methods-Uk* **3**, 646-652 (2011).

## Figure Caption

**Scheme 1.** Reaction of β-lactamase with ceftriaxone (CEF). **(1)** Formation of the enzyme substrate complex by non-covalently binding CEF. **(2)** Nucleophilic attack of the active site residue Ser-70 results in rearrangement of double bonds, and ultimately leads to the opening of the β-lactam ring (blue arrow points to the bond to be cleaved), and the detachment of the release group (R). **(3)** Covalent bond formation between Ser-70 and a shortened species (CFO). Note the double bond Δ. **(4)** The double bond may react with water to form an alcohol (OH). Evidence for all four intermediate species is found in our experiments. Species (4) is further hydrolyzed from Ser-70 and leaves the enzyme as product.

**Figure 1**. Overview of BlaC as determined in the shards crystal form at 500 ms. The mFo-DFc SA-omit electron density is shown for the bound CFO in green (contour level: 2.5 σ). Electron density of an additional, stacked ceftriaxone molecule near the active site is shown in dark green (contour level: 2 σ). **(a)** The BlaC subunits A-D displayed in blue, yellow, green and light yellow, respectively. Amino acid residues which interact with the stacked CEF are labeled. Panels **(b)** and **(c)** show enlarged views of the active sites of subunits B and D, respectively. Arg 126 and Tyr 127 to which the respective stacked CEF molecules are bound are shown. Some important distances are also displayed (stacked molecules are also observed at the other time delays in the shards crystal form but not in the needles).

**Figure 2.** Ceftriaxone electron density in the active site of BlaC in various crystal forms (shards and needles), and at various time delays. The electron density is interpreted by different ceftriaxone species: The main species is displayed in blue, the minor species in gray. For the shards crystal form (panels in the first two columns) mFo-DFc SA-omit density (green) contoured at 2.5 σ is shown. For the needles (panels in the third column), SA omit maps were calculated using extrapolated structure factors (see text) with N=9 for 30ms and 100ms delays, N=6 for the 500ms and N=5 for the 2 s delays. Time-delays are arranged from top (30ms) to bottom (2 s). The first column shows the catalytic cleft in subunit-B of BlaC in the shards crystal form and the second column that of BlaC subunit

D. The third column shows the same BlaC region in the monomeric needle crystal from. Black arrows show the electron density of a covalently bound acyl adduct (see Fig. S2 for details). **(a,b,c)** Formation of the ES complex at 30ms. The full length CEF model (blue) is displayed in the active site. The ES complex can be observed at the same time delay regardless whether needles or shards (both subunits) are investigated. **(d,e, f)** Early phases of the formation of a covalently bound CEF adduct observed at 100ms. The full length CEF model (blue) is displayed together with the minor CFO species (gray), where the β-lactam ring is open and attached to Ser-70 in subunit-B (shards crystal form, panel d) and the needles crystal form (panel f). No covalently bound adduct formation is observed in the shard crystal form subunit D (panel e). **(g,h,i)** Fully cleaved and covalently bound adduct (CFO in blue) formation in the active site at 500 ms. A small contamination of full length CEF (gray) is observed. The red arrow points to electron density that may favor the interpretation by an OH group, rather than assuming a double bond. **(j,k,l)** A mixture of the non-covalently bound, full length CEF and covalently bound CFO is observed in the shards crystal form (both subunits) at 2s, while the electron density in the needle crystal form favors only the full length CEF species.

**Figure 3.** Concentration profile of the catalytic BlaC reaction with CEF as simulated with realistic parameters and the kinetic mechanism (1). The solid lines are calculated with $\tau_D$ = 15 ms, the dashed lines with $\tau_D$ = 1.5 ms. Black lines: free enzyme (E). Green lines: enzyme substrate complex (ES). Blue lines: enzyme-product complex (EP), acyl intermediate (CFO). Red lines: product P, CFO released from the enzyme. Black dots: observed time-delays after mixing.

## Schemes and Figures

## Scheme 1.

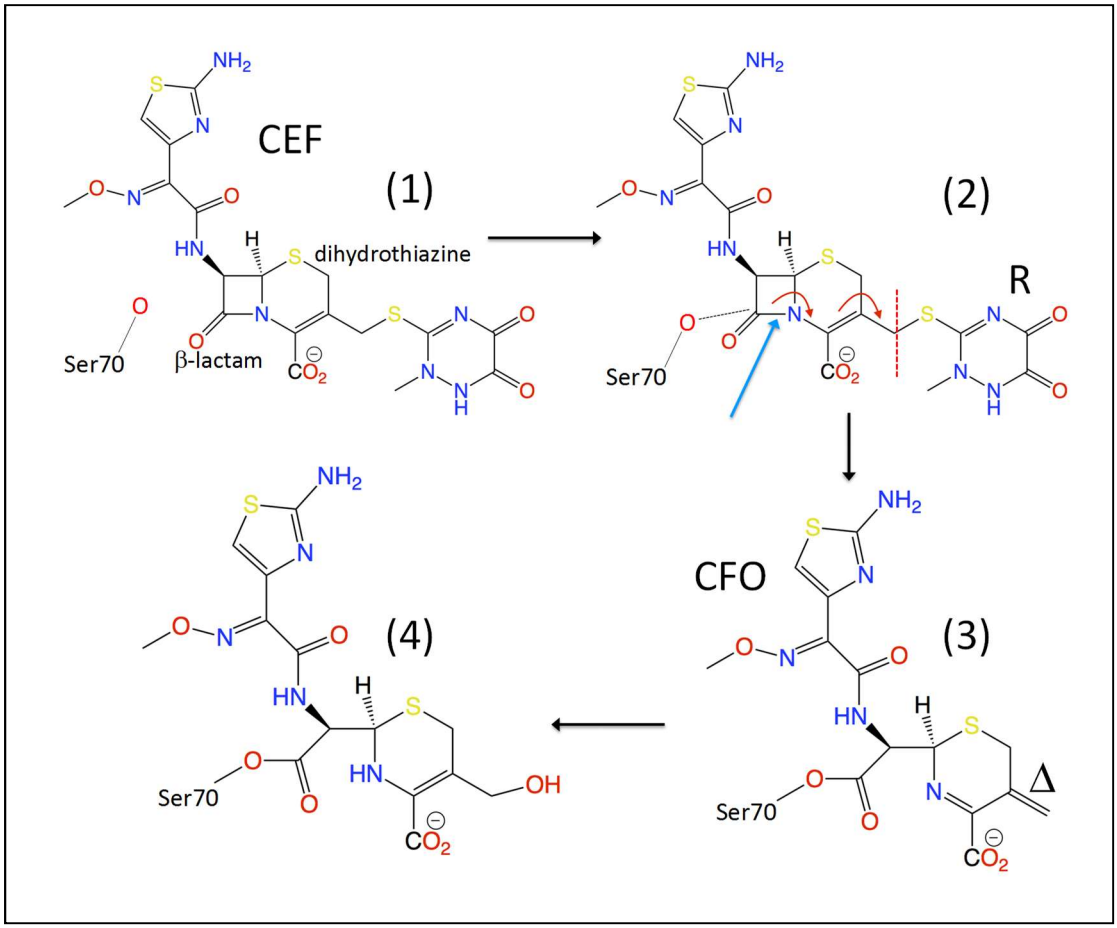

**Figure 1.**

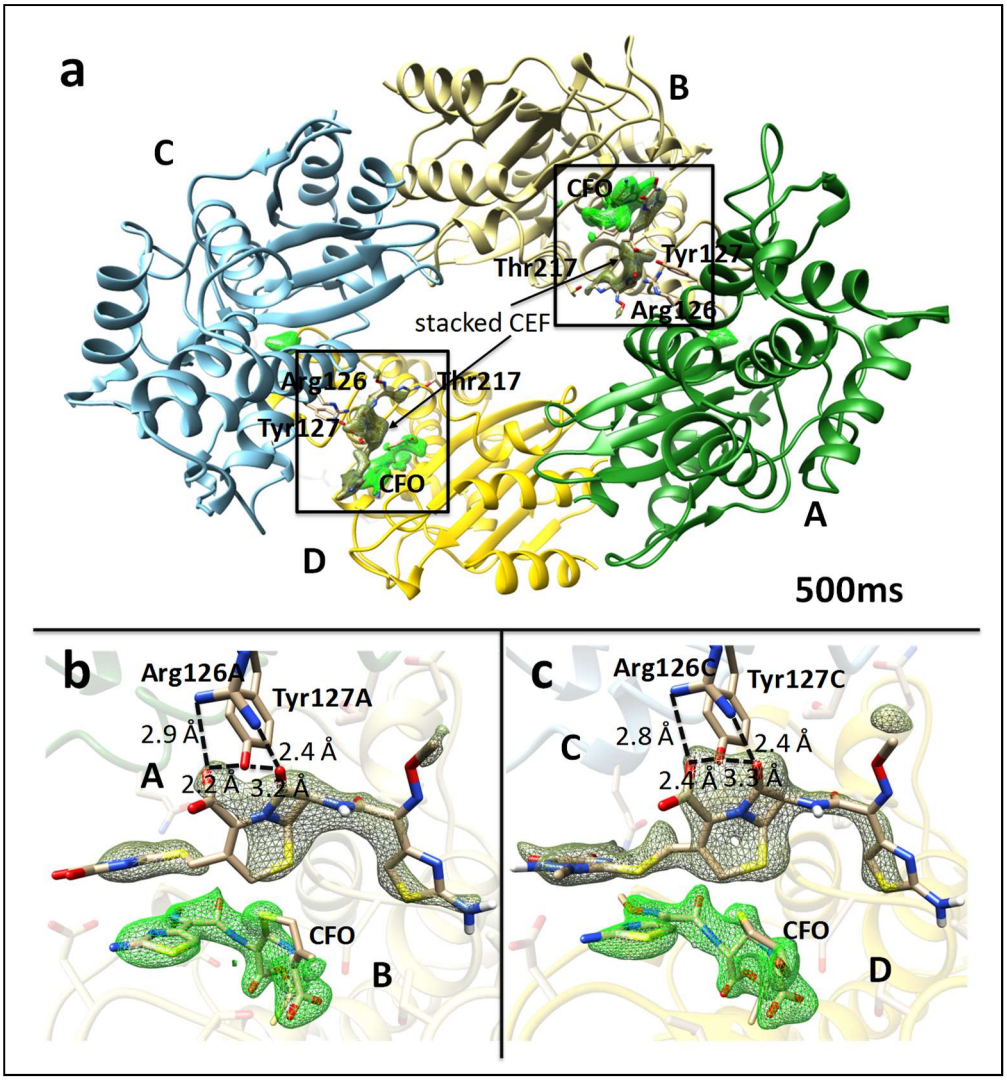
a
B
C
CFO
Thr217
Tyr127
Arg126
stacked CEF
Arg126
Thr217
Tyr127
CFO
A
D
500ms
b
Arg126A
Tyr127A
2.9 Å
2.4 Å
A
2.2 Å
3.2 Å
CFO
B
c
Arg126C
Tyr127C
2.8 Å
2.4 Å
C
2.4 Å
3.3 Å
CFO
D

**Figure 2.**

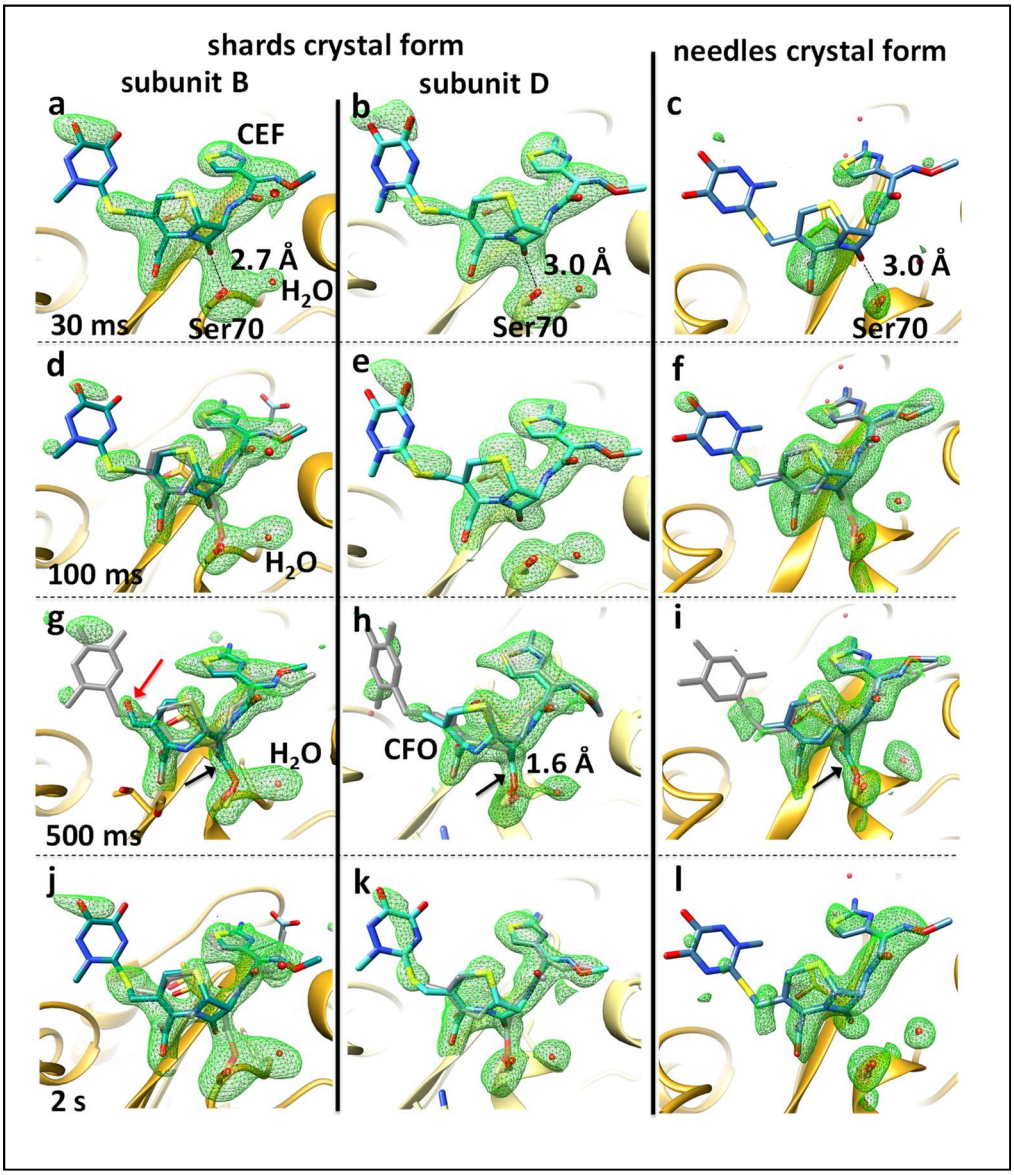
shards crystal form
needles crystal form
subunit B
subunit D
a
b
c
CEF
2.7 Å
$H_2O$
3.0 Å
3.0 Å
30 ms
Ser70
Ser70
Ser70
d
e
f
100 ms
$H_2O$
g
h
i
$H_2O$
CFO
1.6 Å
500 ms
j
k
l
2 s

**Figure 3.**

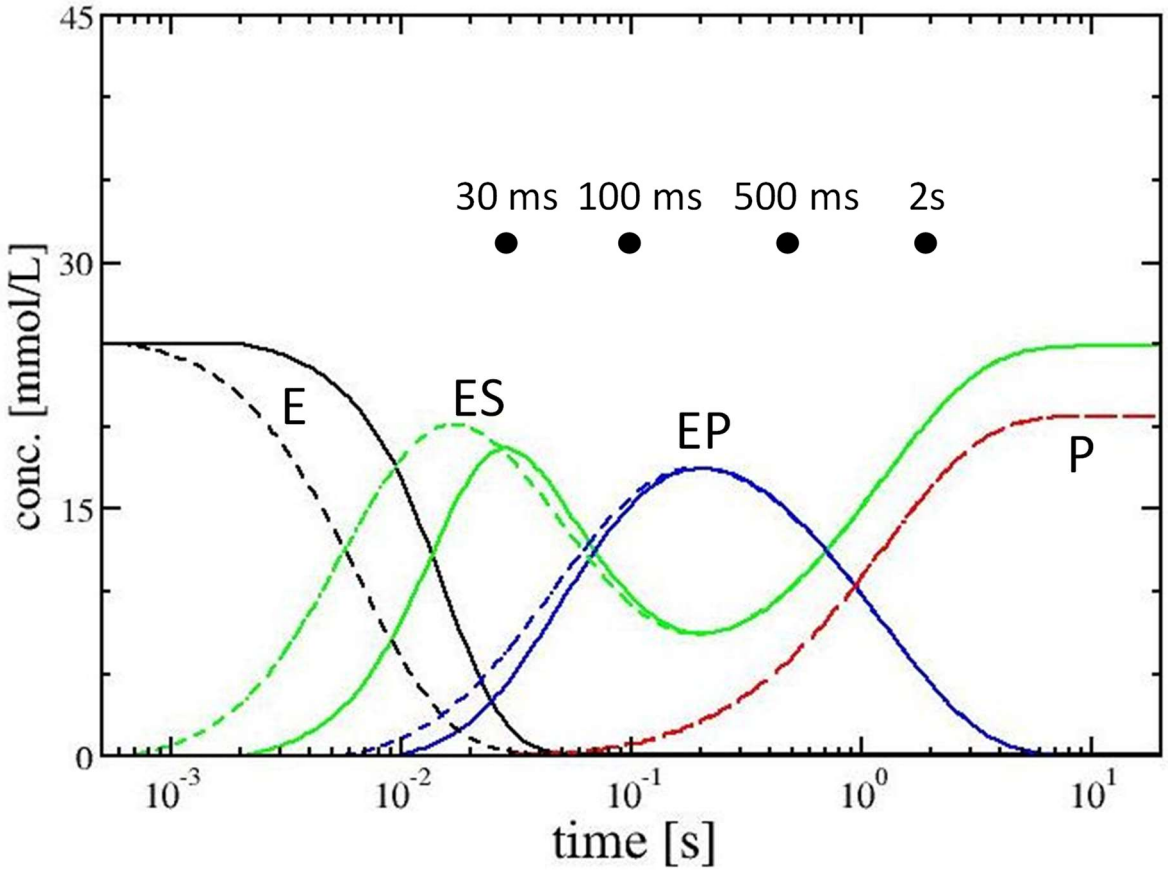
45
30
15
0
conc. [mmol/L]
30 ms
100 ms
500 ms
2s
E
ES
EP
P
$10^{-3}$
$10^{-2}$
$10^{-1}$
$10^{0}$
$10^{1}$
time [s]

# Supplementary Materials for

## Authentic Enzyme Intermediates Captured "on-the-fly" by Mix-and-Inject Serial Crystallography

Jose Olmos[#,a], Suraj Pandey[#,b], Jose M. Martin-Garcia[#,c], George Calvey[d], Andrea Katz[d], Juraj Knoska[e,f], Christopher Kupitz[b], Mark S. Hunter[g], Mengning Liang[g], Dominik Oberthuer[e], Oleksandr Yefanov[e], Max Wiedorn[e,f], Michael Heyman[h], Mark Holl[c], Kanupriya Pande[i], Anton Barty[e], Mitchell D. Miller[a], Stephan Stern[e], Shatabdi Roy-Chowdhury[c], Jesse Coe[c], Nirupa Nagaratnam[c], James Zook[c], Tyler Norwood[b], Ishwor Poudyal[b], David Xu[a], Jason Koglin[g], Matt Seaberg[g], Yun Zhao[c], Saša Bajt[j], Thomas Grant[k], Valerio Mariani[e], Garrett Nelson[l], Ganesh Subramanian[l], Euiyoung Bae[m], Raimund Fromme[c], Russel Fung[b], Peter Schwander[b], Matthias Frank[n], Thomas White[e], Uwe Weierstall[i], Nadia Zatsepin[i], John Spence[i], Petra Fromme[c], Henry N. Chapman[e,f,o], Lois Pollack[d], Lee Tremblay[p], Abbas Ourmazd[b], George N. Phillips, Jr.[a], Marius Schmidt[b,*]

[a]Department of BioSciences, Rice University, 6100 Main Street, Houston, Texas 77005, USA
[b]Physics Department, University of Wisconsin-Milwaukee, 3135 N. Maryland Ave, Milwaukee, Wisconsin 53211, USA
[c]School of Molecular Sciences and Biodesign Center for Applied Structural Discovery, Arizona State University, Tempe, Arizona 85287-1604, USA
[d]Department of Applied and Engineering Physics, Cornell University, 254 Clark Hall, Ithaca, New York 14853, USA
[e]Center for Free-Electron Laser Science, DESY, Notkestrasse 85, 22607 Hamburg, Germany
[f]University of Hamburg, Luruper Chaussee 149, 22761 Hamburg, Germany
[g]Linac Coherent Light Source, Stanford Linear Accelerator Center (SLAC) National Accelerator Laboratory, 2575 Sand Hill Road, Menlo Park, California 94025, USA
[h]Max Planck Institut fuer Biochemie, Am Klopferspitz 18, 82152 Planegg, Germany
[i]Lawrence Berkeley National Lab, 1 Cyclotron Road, Berkeley CA 94720
[j]Photon Science, DESY, Notkestrasse 85, 22607 Hamburg, Germany
[k]University of New York Buffalo, Hauptman-Woodward Institute, 700 Ellicott St, Buffalo, NY 14203, USA.
[l]Department of Physics, Arizona State University, Tempe, Arizona 85287, USA
[m]Department of Agricultural Biotechnology, Seoul National University, Seoul 151-921, Korea
[n]Lawrence Livermore National Laboratory, Livermore, CA 94550, USA
[o]Centre for Ultrafast Imaging, Luruper Chaussee 149, 22761 Hamburg, Germany
[p]4Marbles Inc., 1900 Belvedere Pl, Westfield, Indiana 46074, USA

**This file includes:**

Materials and Methods

SupplementaryText

Figs. S1 to S4

Tables S1 to S2

## Supplemental Material

### Materials and Methods

***1. General Overview.*** Using a continuous-flow mixing apparatus (Fig. S1) we injected active microcrystals of BlaC simultaneously with the β-lactam substrate Ceftriaxone (CEF) into a liquid jet for delivery to the beam as a stream of randomly oriented hydrated nanocrystals *undergoing catalysis*. The catalytic reaction is initiated by solution mixing at the junction of two capillaries(*33*), and the nanocrystals intersected by the X-ray pulse at specific time-points during the reaction. The use of nanocrystals is essential for observation at short times, and for effective and uniform reaction initiation(*24*). The 120 Hz repetition rate of LCLS allowed for the rapid collection of diffraction snapshots at a number of delay times (time-points) after reaction initiation. Accurate reflection intensities were extracted from the snapshots at each time-point by indexing and Monte Carlo type integration (*44, 45*). By phasing the data using the structural model of the apo-BlaC (PDB-entry 2GDN), we obtained, as a function of time, information on distinct chemical intermediates of β-lactam substrates within the active site of BlaC. The BlaC enzyme requires limited conformational changes to execute catalysis, allowing us to observe the full enzymatic reaction within a crystal.

***2. Crystal forms:*** Cloning, overexpression and purification of M. tuberculosis BlaC has been performed as described (*26*). BlaC was crystallized in the shard-like crystal form as described earlier (*26*). The crystallization conditions were varied slightly to avoid the growth of larger crystals that otherwise need to be crushed to be suitable for 'mix-and-

inject serial crystallography' (MISC) experiments. An additional crystals form was obtained from a different crystallization condition using the free interface diffusion (FID) method (Kupitz et al, 2014). In a 1.5 mL eppendorf, 250 µL of a precipitant solution (35% PEG 1000, sodium acetate pH 5.0), were slowly added drop wise through 250 µL of a protein solution at 10 mg/mL. Needle-shaped crystals grow at room temperature in about 48 h. The microcrystalline sample was highly monodisperse with crystal sizes between 3 and 5 µm as demonstrated by dynamic light scattering. Microcrystal quality was assessed with SONICC (second order of non-linear imaging of chiral crystals). The suspension showed an intense SONICC signal demonstrating the crystallinity of the sample. X-ray powder diffraction was used as a quality test to verify the existence of diffracting crystals. A very high density pellet of micro-crystals was transferred to a transparent plastic capillary (MITIGEN). A small amount of precipitant solution was kept to prevent crystals from drying out. The capillary was mounted onto a regular goniometer base and data were collected for 3 min on a home source. Intense powder rings were observed up to 7A. Weaker rings were also observed to extend up to approximately 4A.

***3. Injectors.*** The mixing injectors used in this experiment were based on the design by Calvey et al.(*31*) shown in Fig. S1. In these devices, crystal suspension and a buffer (either 1 mol/L Na-phosphate or Na-acetate, pH5) containing 200 – 300 mmol/L CEF flow in coaxial capillaries. The flows are combined and forced into a constriction, thinning the crystal flow to a narrow jet and allowing rapid CEF diffusion. By varying the length of the device, the sample and buffer flow rates, or placing an expanded region after the constriction, we were able to probe timescales ranging from 30 ms to 2000 ms. Two HPLC pumps (SHIMADZU LC-20AD) drove the flow. Crystals were held in a custom reservoir

built by CXI staff, while buffer was held in a larger reservoir (KNAUER VARILOOP), allowing to flow water through the HPLC pump without diluting either sample or buffer. A pressure controller (PROPORTION-AIR GP1) was used to regulate helium pressure in the device. For each condition, the solution is considered mixed when the CEF concentration exceeds 40 mM, sufficiently high to cause rapid binding. The reported mixing times are the time for the concentration around the average crystal to reach this threshold, with upper and lower bounds given for the first and third quartile. In these calculations, the crystals are assumed to be much smaller than the focused jet, and fluctuations in flowrate are neglected. The mixing times for each time point are reported in Tab. S1. The delay time is defined as the time that the reaction is allowed to proceed after mixing. During this time, the crystals traverse the device before being probed by the x-ray beam. Uncertainty in the delay time results from errors in the sample and buffer flow rates (which come from the factory specifications for the Shimadzu LC-20AD HPLC pumps that we used to drive the flows) and from small variations in the diameters and lengths of capillaries used to make the mixing injectors. Mixing injectors were designed so that the delay time slightly exceeded the nominal timepoint to allow for additional time for the ceftriaxone to diffuse into crystals. Tab. S1 lists the delay times and flow parameters for different timepoints.

***4. Data collection, data analysis and structure determination.*** Serial femtosecond crystallography (SFX) experiments were performed at the Coherent X-ray Imaging (CXI) instrument (*46*). Microcrystals were mixed with the antibiotic ceftriaxone before injection into vacuum using a mixing jet injector described above that allowed millisecond time resolution. Diffraction patterns were recorded on a Cornell-SLAC Pixel Array Detector

(CSPAD) operating at 120 Hz to match the X-ray pulse frequency. Data for shards and needles were analyzed in an identical fashion. Cheetah (*47*) was used to filter out diffraction patterns containing Bragg reflections. These patterns were indexed and integrated using the CrystFEL (version 0.6.2) program suite (*45, 48*). Partial intensities were scaled and merged using linear and Debye Waller factor scale factors. Data statistics is listed in Tab. S2. The BlaC structures were solved for the needles and shards using molecular replacement by PHASER (*49*). For the shards, the tetrameric structure determined by Kupitz et al. (2017) was used as initial model. For the monomeric structure in the needles subunit D of the tetramer was extracted and used as a search model. Reference structures $S_{ref,n}$ and $S_{ref,s}$ were determined for the needles and shards, using the respective 'unmixed' data for both crystals forms. To determined structural changes after mixing, difference maps were determined. For the shards unit cell changes on the order of 2 Å and larger were observed after mixing. This prevents the calculation of isomorphous difference maps. With the needles however, unit-cell changes were not observed (compare Tab. S2) and isomorphous difference maps can be calculated. Accordingly, two different strategies were followed to analyze the two types of data.

(i) Structures for the shards crystal form: Since isomorphous difference maps could not be calculated, structural interpretation has been based on omit difference maps. The tetrameric reference model was refined using simulated annealing (SA) in 'PHENIX' against the observed $\left|F_t^{obs}\right|$. For this refinement water and phosphate molecules residing in the active sites of all subunits were removed. In addition Ser-70 was replaced by a glycine (Gly-70) in subunits B and D. The structure was heated to 5000 K (default) and

slowly cooled to 300 K. As a result, a model of the apo-protein without any ligands in the active site was obtained. After the refinement, $mF_o$-$DF_c$ omit difference maps $\Delta\rho_t^{omit}$ were calculated for each time point t, where the $F_o$ correspond to the $\left|F_t^{obs}\right|$ and the $F_c$ are determined from the refined (partial) model, m is the figure of merit and D is a coordinate error dependent weighting term (*50, 51*). The resulting omit-map is essentially free of phase bias towards the ligand free 'unmixed' structure. Strong electron density appeared in subunits B and D that was reminiscent of CEF molecules. In subunits A and C, the electron density of only the phosphate and the water molecules re-appeared, a result that was also previously reported (*26*). Hence, the structures of the catalytic clefts in these subunits A and C were restored back to the reference. The $\Delta\rho_t^{omit}$ in the catalytic clefts of subunits B and D was exceptionally strong at all time delays. Appropriate CEF species (Scheme 1) were placed in the positive $\Delta\rho_t^{omit}$ and initially real-space refined in 'Coot' using adequate crystallographic information files (CIF), which define the geometry and provide restraints. CIF files were generated for the full length Ceftriaxone (CEF) as well as an open form with the release group split off (CFO) as previously described (*26*), compare also Scheme 1. One oxygen of the open lactam carboxyl in CFO was removed and the carboxyl carbon was connected to the Ser70-$O_g$ with a weak distance restraint of 1.6 Å. At all time points, either CEF, CFO (bound to Ser-70) or a mixture of both were observed. Their structures were first refined in real space against the $\rho_t^{ext}$ in 'Coot'. Mixtures of full length, non- covalently bound CEF configurations and Ser-70 bound, open forms (CFO) were refined together in 'PHENIX'. Note, that CFO was replaced at 500 ms in subunit B with a species displaying an alcohol (Fig. 2g, Scheme 1d) instead of the double bond $\Delta$, the structure of which was refined as described. Further refinement

including occupancy refinement of the two species was performed with 'PHENIX' (*52*) against the $|F_t^{ext}|$. Since a large volume of electron density is shared by CEF and the shorter CFO, occupancy refinement is not reliable. Numbers obtained reflect the fact that the two molecules are present. Essentially complete ligand occupancy is reached at all time delays. Therefore, a potential presence of an unmixed BlaC species was not taken into account during the refinement. The stacked CEF ($CEF^{stack}$) has been added to the last phase of the refinement. The release group (the large dioxo-triazin ring) is π–π stacking with the small amino-thiazol ring of the CEF species in the active site resulting in an antiparallel alignment. Distance between the rings are on the order of 3.5 Å. However, as mentioned in the text, the main interactions are with Tyr-127 (between Tyr-127$O_\eta$ and $O_l$ of the $CEF^{stack}$ dihydrothiazine carboxyl) and Arg-126 (between Arg-126$N_\varepsilon$ and $O_l$ of $CEF^{stack}$-$O_l$) of the adjacent (inactive) dimer subunit (see Fig. 2b,c in the main text). $CEF^{stack}$ is preoriented this way. In order to access the active site, $CEF^{stack}$ only has to flip by 180°, which may be initiated when the CFO species leaves the active site.

(ii) Structures for the needle crystal form: Difference structure factor amplitudes $\Delta F_t^{iso}$ were calculated for each time point t by subtracting the observed reference structure factor amplitudes $|F_{ref}^{obs}|$collected with no CEF present from the time-dependent structure factor amplitudes $|F_t^{obs}|$. From the $\Delta F_t^{iso}$ and the phases derived from $S_{ref,n}$, isomorphous difference maps were calculated. In order to model the BlaC structure including (a potentially modified) CEF ligand, conventional electron density maps $\rho_t^{ext}$ were calculated where the ligand occupation was extrapolated to 1.0. Extrapolated structure factors $F_t^{ext}$

were calculated by adding the $\Delta F_t^{iso}$ N times (see Tab. S2) to the calculated structure factors derived from $S_{ref,n}$. Extrapolated electron density $\rho_t^{ext}$ was derived from the $F_t^{ext}$. The structures of appropriate CEF derivatives (see above and Scheme 1) were inserted using 'Coot' (*53*). At all time points, either CEF, CFO (bound to Ser-70) or a mixture of both were observed. Their structures were first refined in real space against the $\rho_t^{ext}$ in 'Coot'. Further occupancy refinement was performed as described above (i).

**Supplementary Text**

***Enzyme Kinetics.*** The Michealis constant $K_m$ is on the order of 500 x $10^{-6}$ mol/L for BlaC with CEF, and $k_{cat}$ is 0.8 $s^{-1}$ (*37*). The $k_{off}$ rate coefficient of dissociation of substrate from the active site is unknown. When the $k_{off}$ rate coefficient is assumed to be equal to the $k_{cat}$ rate coefficient, the $k_{on}$ rate coefficient for the binding of CEF can be estimated from: $k_{on} = \frac{2xk_{cat}}{K_m} = \frac{2x0.8}{500\ x\ 10^{-6}}\ L\ mol^{-1}s^{-1} = 3200\ L\ mol^{-1}s^{-1}$. Characteristic diffusion times of CEF with a diffusion coefficient of 2.3 x $10^{-6}$ $cm^2/s$ in water (*54*) into 2/4/10 x 2/4/10 x 2/4/10 $\mu m^3$ crystals are 0.6ms/2.4 ms/15ms (*24*). The time dependent concentrations of species along the enzymatic pathway were simulated by numerically integrating the coupled differential equations of the simple kinetic mechanism shown in (1) using the above rate coefficients which reproduce the known $K_m$. Note, that formation of the EP complex (acyl intermediate) is irreversible due to the cleavage of the release group $R_2$ from CEF. In the simulation $k_2$ was assumed to be 15 1/s.

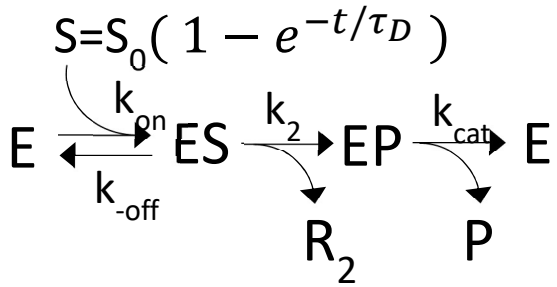


(1)

The substrate concentration S in the crystal is determined by the outside substrate concentration $S_0$ (50 mmol/L in the simulation) and the characteristic diffusion time $\tau_D$. S is fed to the free enzyme E and bound to the enzyme with $k_{on}$. The total enzyme concentration was set to 25 mmol/L. Results are shown in Fig. 4. $\tau_D$ was varied from 15 ms (solid lines) to 1.5 ms (dashed lines). Sufficient accumulation (occupation) of the enzyme substrate complex (ES, green) is achieved after 30 ms even with the larger crystals and corresponding longer diffusion times (Fig. 3), which agrees with our MISC results. Due to the low $k_{cat}/K_m$ ratio (~ 1.5 x $10^3$ L $mol^{-1}$ $s^{-1}$) CEF is a slow binder. Variations of diffusion times by a factor of 10 (1.5 ms to 15 ms) into the crystals do not play a critical role (Fig. 3), and the MISC experiment becomes robust against crystal size heterogeneities as well as against mixing time jitter (Tab. S1). As expected the ES complex is forming slightly faster with the fast diffusion time, but the kinetics looks essentially the same for both simulated diffusion times. The acyl intermediate (EP, blue) is forming essentially on the same time scale. In our MISC X-ray data we do not see clear evidence of an additional product complex ($EP_2$) where the CFO (CEF with open β-lactam ring, bound to Ser-70) is hydrolyzed (detached) from Ser-70. It appears as if this species leaves the enzyme faster than its formation, and therefore does not accumulate

sufficiently to be detected. Since the ES complex reappears in our MISC data in the steady state on times > 1 s, product inhibition of rate coefficient $k_2$ was assumed by lowering $k_2$ to zero: $k_2 = k'_2(1 - e^{-P_n})$, with $P_n$ the concentration of the released product P divided by 1 mmol/L. Since the concentration of enzyme in the crystal is very high, even only one catalytic cycle produces on the order of 10 mmol/L product (Fig. 4, red line) which may strongly inhibit the reaction. This might be the first evidence for product inhibition of the BlaC reaction which awaits further investigations which are outside the scope of this paper.

**Table S1.** Mixing parameters for each timepoint. The buffer contained 200 – 300 mmol/L CEF in either 1.0 mol/L Na-phosphate (shards crystals form), pH 5, or in 100 mmol/L Na-acetate, pH 5 (needle crystal form).

| Nominal Timepoint (ms) | Mixing Time (ms) | Delay Time (ms) | Sample Flow (μL/min) | Buffer Flow (μL/min) | Constriction Diameter (μm) |
|---|---|---|---|---|---|
| 30 | $5^{+6}_{-3}$ | $42 \pm 2$ | $4.0 \pm 0.5$ | $66.0 \pm 0.6$ | $75 \pm 1$ |
| 100 | $10^{+13}_{-8}$ | $114 \pm 4$ | $10.0 \pm 0.5$ | $70.0 \pm 0.7$ | $75 \pm 1$ |
| 500 | $7^{+10}_{-5}$ | $510 \pm 20$ | $8.0 \pm 0.5$ | $32.0 \pm 0.5$ | $50 \pm 1$ |
| 2000 | $15^{+20}_{-11}$ | $2300 \pm 50$ | $10.0 \pm 0.5$ | $45 \pm 0.5$ | $75 \pm 1$ |

**Table S2.** Data collection and refinement statistics.

**(a) Shards**

| | Reference | 30 ms | 100 ms | 500 ms | 2s |
|---|---|---|---|---|---|
| Hits | 98895 | 35065 | 88413 | 158620 | 39140 |
| Indexed Images | 73170 | 24397 | 79328 | 134583 | 32201 |
| Resolution | 2.45 | 2.75 | 2.15 | 2.20 | 2.30 |
| Spacegroup | P21 | P21 | P21 | P21 | P21 |
| Unit Cell [Å,°] (a,b,c and $\gamma$) | 79.0 97.2 110.6 108.7 | 78.7 96.8 112.6 109.7 | 79.2 96.5 113.7 109.9 | 78.8 96.3 113.5 110.0 | 78.2 95.6 112.3 109.9 |
| Volume [Å$^3$] | 804,442 | 807,597 | 817,098 | 809,346 | 789,415 |
| BlaC/unit cell | 8 | 8 | 8 | 8 | 8 |
| Completeness | 100(100) | 100(100) | 100(100) | 100(100) | 100(100) |
| Multiplicity | 1220.89(103.3) | 526.16(142.0) | 894.63(58.8) | 1363.04(81.3) | 329.82(59.0) |
| SNR | 8.9(2.4) | 6.4(0.9) | 7.1(1.0) | 8.3(0.9) | 5.4(1.1) |
| $R_{split}$ [%] | 9.8(209.4) | 14.2(121.1) | 11.18(111.0) | 9.7(126.3) | 11.9(104.1) |
| CC-half[%] | 99.4(41.1) | 98.6(34.5) | 99.4(37.5) | 99.6(31.0) | 96.8(35.4) |
| | | | | | |
| Refinement | | | | | |
| $R_{cryst}/R_{free}$ [%] | 19.2/24.4 | 19.3/25.0 | 20.9/23.9 | 21.9/25.0 | 23.5/26.6 |
| $^{*B}$CEF/CFO[a] | 0/0 | 70/23[b] | 57/32 | 40/36* | 58/25 |
| $^{*D}$CEF/CFO[a] | 0/0 | 69/24[b] | 54/40 | 38/44 | 51/31 |
| Stacking | no | yes | yes | yes | yes |
| $H_2O$ | 315 | 143 | 499 | 431 | 399 |
| Average B value [Å$^2$] | 48.2 | 51.7 | 42.3 | 37.3 | 36.2 |
| Protein amino acid residues in asym. unit | 265×4 | 265×4 | 265×4 | 265×4 | 265×4 |
| Ligands | 0 | 2+2(stacking) | 2+2(stacking) | 2+2(stacking) | 2+2(stacking) |
| RMSD bond lengths(Å) | 0.008 | 0.010 | 0.008 | 0.008 | 0.008 |
| RMSD bond angles(Deg) | 1.10 | 1.72 | 1.66 | 1.67 | 1.74 |
| PO4 | 4 | 2 | 2 | 2 | 2 |

[a] occupation of full length, intact CEF to covalently bound, open CFO, which has lost $R_2$, after refinement, numbers are rough estimates.
[b] if full occupation with CEF and CFO is not reached, the protein structure represents a mixture of two structures, one with ligand bound, and one with no ligand bound
$^{*B}$ for subunit B
$^{*D}$ for subunit D
* addition of OH instead of the double bond $\Delta$

**(b) Needles**

| | Reference | 30 ms | 100 ms | 500 ms | 2s |
|---|---|---|---|---|---|
| Hits | 171314 | 64507 | 115223 | 141935 | 36606 |
| Indexed Images | 111466 | 34590 | 87580 | 87058 | 23278 |
| Resolution | 1.8 | 1.9 | 1.8 | 1.9 | 2.05 |
| Spacegroup | P21 | P21 | P21 | P21 | P21 |
| Unit Cell [Å,°] (a,b,c and $\gamma$) | 39.6 41.6 69.3 104.8 | 39.5 41.6 69.3 104.8 | 39.6 41.6 69.3 104.9 | 39.6 41.7 69.5 104.9 | 39.6 41.7 69.5 104.9 |
| Volume [$Å^3$] | 110,375 | 110,096 | 110,323 | 110,908 | 110,908 |
| Completeness | 100(100) | 100(100) | 100(100) | 100(100) | 100(100) |
| Multiplicity | 985.3(54.5) | 329.8(26.8) | 831.3(89.0) | 806.0(36.5) | 238.0(27.3) |
| SNR | 9.6 (1.2) | 5.8(0.8) | 9.6(1.6) | 8.6(0.9) | 5.1(1.1) |
| $R_{split}$ [%] | 6.6 (97.0) | 12.2(136.3) | 6.6(72.5) | 8.8(129.1) | 14.0(105.9) |
| CC*[%] | 99.9(75.0) | 99.9(76.1) | 99.9(84.3) | 99.9(68.1) | 99.8(74.8) |
| CC-half[%] | 99.7(39.1) | 99.4(40.4) | 99.7(55.1) | 99.7(30.2) | 99.13(38.8) |
| Refinement | | | | | |
| $R_{cryst}/R_{free}$ [%] | 21.5/24.5 | 20.7/26.2 | 23.0/26.7 | 21.7/26.4 | 20.0/25.0 |
| N[c] | - na - | 9 | 9 | 6 | 5 |
| CEF/CFO[a] | 0/0 | 59/0 | 51/35 | 43/53 | 71/0 |
| Stacking | no | no | no | no | no |
| $H_2O$ | 167 | 203 | 154 | 104 | 175 |
| Average B value [$Å^2$] | 34.7 | 16.9 | 10.5 | 15.7 | 18.3 |
| Protein amino acid residues in asym. unit | 265 | 265 | 265 | 265 | 265 |
| Ligands | 0 | 1 | 1 | 1 | 1 |
| RMSD bond lengths(Å) | 0.008 | 0.007 | 0.007 | 0.003 | 0.008 |
| RMSD bond angles(Deg) | 1.06 | 1.57 | 1.74 | 1.49 | 1.57 |

[c]If N does not extrapolate to 100 % occupation, a fraction of reference structure is present. This is ignored in the refinement.
na: not applicable

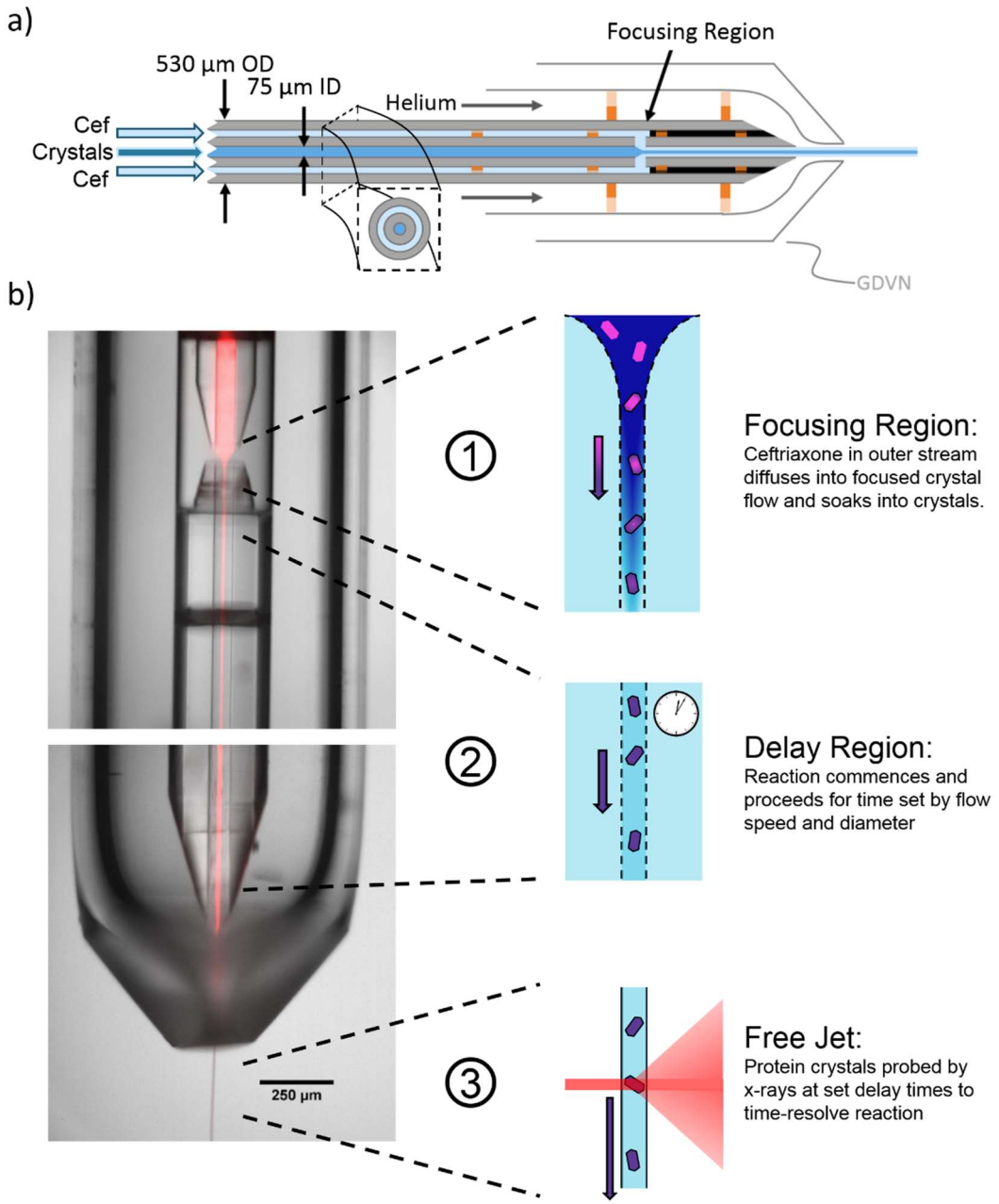


**Figure S1**. a) Schematic of short timepoint mixing injector. Capillary dimensions vary by timepoint. b) Composite image of fluorescent dye flowing through the sample capillary and water flowing through the buffer capillary. Cartoons illustrate the operating principle of each region of the device.

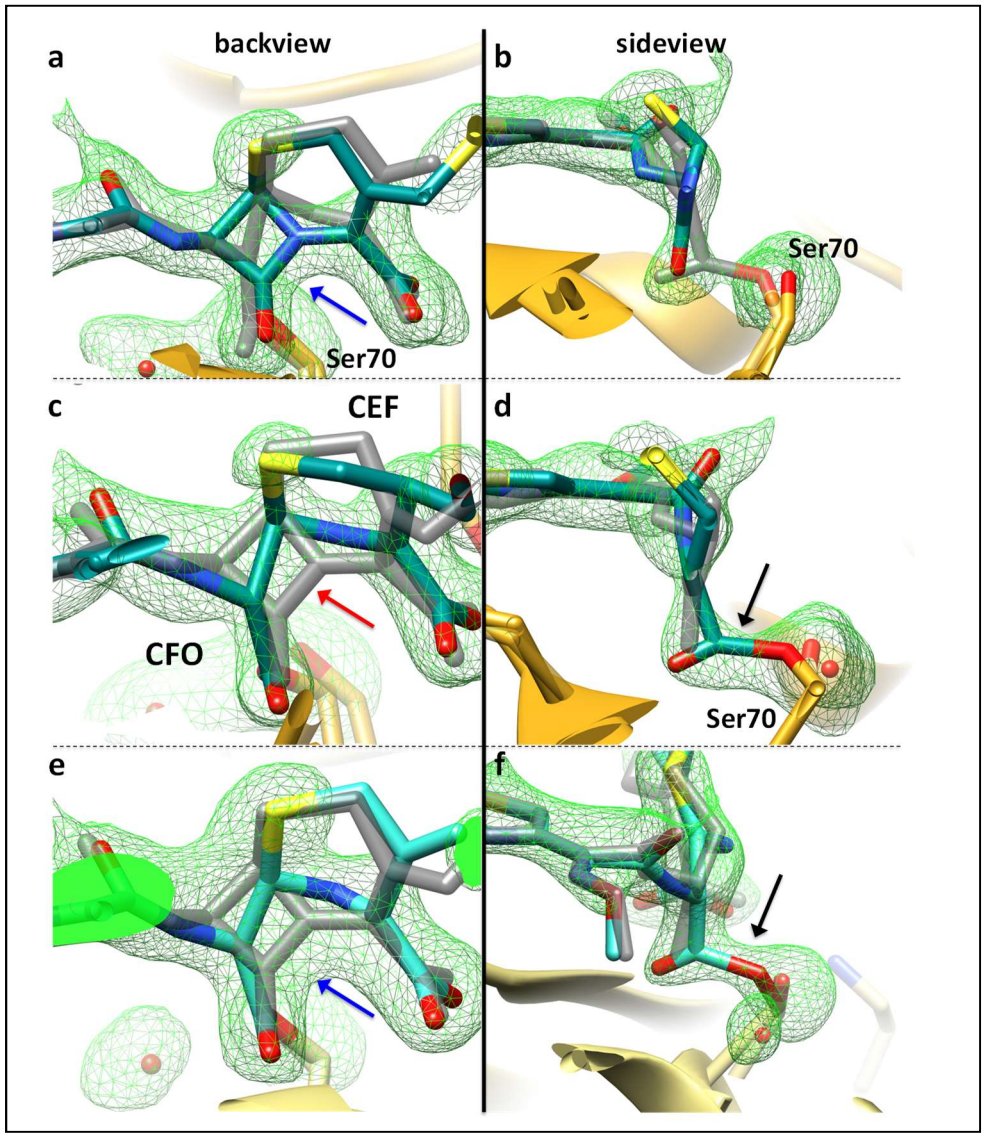


**Figure S2.** Selected views on the CEF binding site in the BlaC shards crystal form at various time delays. mFo-DFc SA omit electron density (green) contoured at 2.5σ. The first column shows the view on β–lactam ring from the backside in relation to Fig. 1 in the main text. The second column shows the side view to demonstrate cleavage of the lactam ring, and the covalent bond formation to Ser-70. The electron density is interpreted with two species (major species in blue, minor species in gray). **(a, b)** Electron density at 100ms in the BlaC shards crystal form, subunit B. The non-covalently bound, full length CEF is the main species. The closed, uncleaved β-lactam ring nicely fits the electron density (a, blue arrow). The electron density between SER 70 and the open lactam ring is weak (b). If any, the concentration of the covalently bound acyl adduct (CFO) is low. **(c, d)** Electron density at 500ms in the BlaC shards crystal form, subunit B. A covalently bound species (CFO), where the β-lactam ring is opened, and the release group is split off, is the main species (blue). **(c)** The closed β-lactam ring poorly fits the electron density (red arrow), and the electron density is interpreted by an open lactam ring (c). Strong

electron density between SER 70 and the carboxyl of cleaved lactam ring indicates a covalent bond (d, black arrow). **(e, f)** Electron density at 500ms in the BlaC shards crystal form, subunit D. The full length CEF, and the CFO acyl adduct are present approximately at equal proportions. The β-lactam ring fits nicely in the electron density (blue arrow), which can be interpreted by an uncleaved, full length CEF structure (e). However, in (f), strong electron density between the SER 70 and the cleaved open lactam ring (black arrow) indicates mixing in of a covalently bound CFO species.

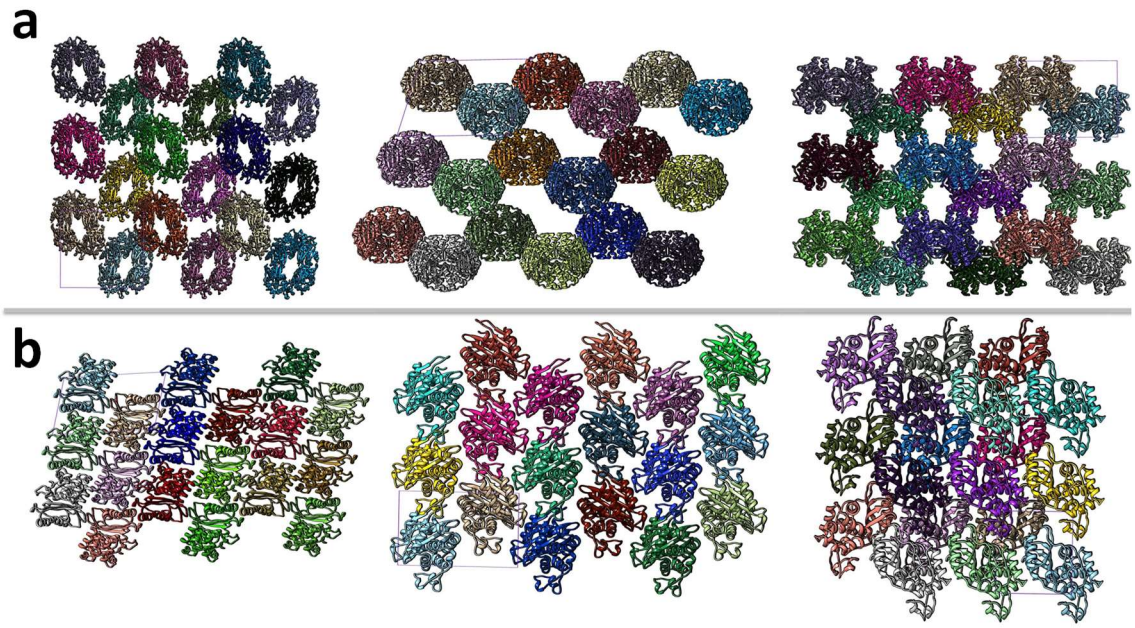


**Figure S3.** Crystal packing of BlaC in different crystal forms viewed from three different directions normal to the unit cell surfaces. 27 unit cells (three each in the directions along the unit cell axes) are displayed and viewed in orthographic projection. One of the unit cells is outlined for each respective view with faint purple lines. The unit cell volume of the shards is on the order of 805,000 $Å^3$ with 8 subunits in the unit cell (one tetramer/asymmetric unit). The concentration of BlaC subunits is 16 mmol/L. The unit cell volume of the needles is about 110,600 $Å^3$ with 2 monomers in the unit cell. The concentration of BlaC is 30 mmol/L. (a) Shards, displaying large solvent channels in all 3 directions. (b) Needles, solvent channels are substantially smaller. Note, the display is not to scale. BlaC monomers in (b) appear larger than BlaC subunits in (a).

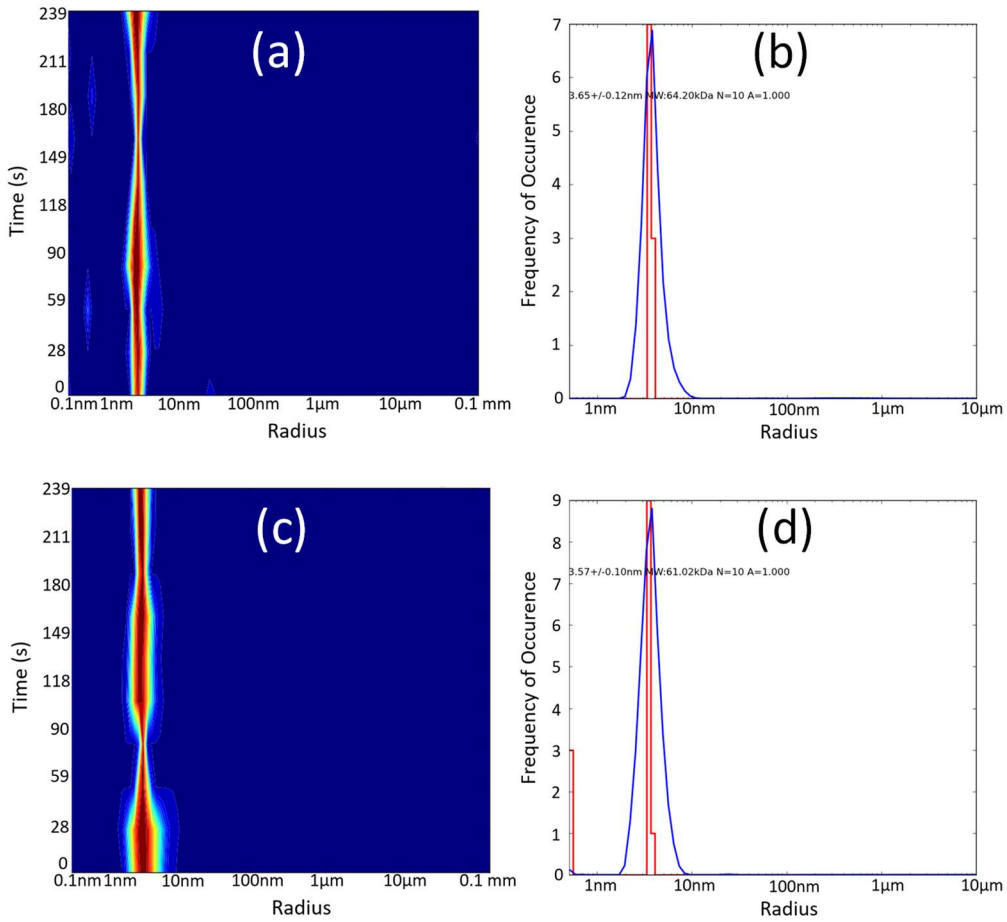


**Figure S4.** Dynamic Light Scattering on BlaC at 40 mg/mL at pH 5 using a DynaPro NanoStar M3300 (WYATT TECHNOLOGY). A 120 mW laser of 660 nm was used as the light source. For each measurement, the number of acquisitions was 10 and each acquisition time was 20 s. All measurements were carried out at 20 °C. (a) and (b) in 100 mmol/L Na-acetat buffer, (c) and (d) in 100 mmol/L Na-phosphate buffer. (a) and (c) show size distribution over time. (b) and (d) show the radius distribution. A very monodisperse species is present. From (b) and (d) accurate molecular weights can be calculated: (a) 64.2 kDa, (b) 61.0 kDa. The mass of a BlaC momomer is 30.6 kDA (*1*). The BlaC exists as a dimer at this pH in both buffers. Essentially the same result is obtained with 20 mg/mL BlaC.